UHBR OPEN-TEST-CASE FAN ECL5/CATANA: NUMERICAL INVESTIGATION NEAR THE STABILITY LIMIT INCLUDING AERODYNAMIC MISTUNING

Anne-Lise Fiquet, Xavier Ottavy, Christoph Brandstetter

UHBR OPEN-TEST-CASE FAN ECL5/CATANA: NUMERICAL INVESTIGATION NEAR THE STABILITY LIMIT INCLUDING AERODYNAMIC MISTUNING

Anne-Lise Fiquet, Xavier Ottavy and Christoph Brandstetter
Univ. Lyon, École Centrale de Lyon, CNRS, Univ. Claude Bernard Lyon 1,
INSA Lyon, LMFA, UMR5509, 69130, Écully, France
Email: christoph.brandstetter@ec-lyon.fr

ABSTRACT

Non-synchronous blade vibration (NSV) has received enormous attention in turbomachinery research, since it can be safety critical and its occurrence is less predictable than typical aeroelastic instabilities such as flutter. Typical for front stages of core compressors, NSV arises due to the propagation of one or multiple aerodynamic disturbances, traveling around the circumference and locking-in with structural blade vibration modes. Recent studies have shown, that modern low-speed fan architectures are also susceptible for this type of instability. With a specific focus on such aeroelastic instabilities, the open-test-case fan stage ECL5 has been designed by Ecole Centrale de Lyon. It is representative of near-future UHBR fan concepts with carbon-fibre composite blades. To prepare the experiments planned for 2022, unsteady full-annulus simulations have been carried out. Depending on rotation speed, the emergence of aerodynamic disturbances traveling around the circumference at a typical convective speed is observed, such as reported in studies on NSV on different configurations. These aerodynamic disturbances are identified as a possible source for non-synchronous vibration. At design conditions, an unstable aerodynamic behavior is observed, with part-span stall cells developing within the operating range predicted by RANS simulations. A study of intentional aerodynamic mistuning, in form of an alternating leading edge pattern is presented. At design speed, influence on steady performance and the onset of part-span stall is observed. At part-speed, the evolution of small-scale vortical disturbances, which can be responsible for the onset of NSV is affected significantly, providing a possible method to suppress NSV.

NOMENCLATURE

Δp	non-synchronous pressure fluctuation [Pa]
ΔS	unsteady specific Entropy [J/(kgK)]
P_t	Total pressure [Pa]
T_t	Total temperature [K]
M_{is}	Isentropic Mach Number [-]
M_{rel}	Relative Mach Number [-]
N_a	Aerodynamic wave number [-]
N_b	Number of rotor blades [-]
Ω_r	Angular shaft velocity [rad/s]
Ω	Angular velocity [rad/s]
T_r	Rotational period [s]
f_r	Rotational frequency [Hz]
T_{fan}	Fan blade passing period [s]
$\dot{m}$	Massflow rate [kg/s]
r	Radius [m]
H	Channel height [%]
V_x	Axial velocity [m/s]
V_r	Radial velocity [m/s]
NSV	Non-Synchronous Vibrations
OGV	Outlet Guide Vane
OP	Operating point
UHBR	Ultra High Bypass Ratio
$.^S$	Stationary frame of reference
$.^R$	Rotating frame of reference
$.a$	Aerodynamic disturbance

accepted manuscript: Fiquet, A.L., Ottavy, X. and Brandstetter, C. "UHBR open-test-case fan ECL5/CATANA: Numerical investigation near the stability limit including aerodynamic mistuning." Proceedings of the ASME Turbo Expo 2022: Turbomachinery Technical Conference and Exposition. Rotterdam Ahoy Convention Centre, Rotterdam, The Netherlands. June 13 – 17, 2022

1 Introduction

Over the last decades, extensive research has been carried out on unsteady aerodynamic phenomena limiting the stability of high-speed axial compressors and low-speed fans. Accurate prediction at off-design conditions remains difficult as these phenomena can be driven by coupled aerodynamic, acoustic and mechanical effects. Already, the aerodynamic prediction capabilities of established simulation methods have proven inaccurate for novel low-speed fan designs at throttled conditions [1]. Research has focused on the evolution of aerodynamic disturbances, causing either significant loss of aerodynamic performance at highly loaded conditions or aeroelastic problems. Propagating aerodynamic phenomena can become critical if off-resonant non-synchronous excitation causes limit-cycle oscillations of blades, limiting component life, or worse, resonance with blade eigenmodes leads to immediate damage. Numerous experimental cases have been reported in literature where aerodynamic disturbances interact with the structure, causing large amplitude blade vibrations [1–8].

Rotating stall is the most-studied phenomenon which occurs near the stability limit with a significant shift in operating conditions due to flow separations on the blade suction surface, and forming propagating cells. This can be typically attributed to a loss in stage pressure ratio, depending on the size of the stall cells. Phenomenologically, rotating stall is self-sustained, and can exist without blade vibration, however, Zhao et al. [9] reported influence of large vibration amplitudes on the evolution of stall cells. Precursors of rotating stall in form radial vortices are reported further from the stability limit at stable operating conditions [10–13]. These disturbances can adapt their phase and rotation speed with a coherent structural vibration pattern (lock-in), leading to significant blade vibration, discussed under the term Non-Synchronous Vibration (NSV) [14]. This specific phenomenon was typically reported for high-speed compressors [1, 3, 6, 8], but the study in [1] has shown a similar phenomenon in a low-speed composite fan. The aerodynamic design is comparable to the test case discussed in the present paper and hence of general interest for future low-speed architectures. The study in [15] has shown that specific types of asymmetry, either in form of structural (frequency) mistuning or geometric blade-to-blade variations (aerodynamic mistuning) can be successful to suppress NSV, building the basis for the study presented here.

To provide a test case with representative geometries of near-future UHBR fan concepts without industrial restrictions, the open-test-case fan stage ECL5 has been designed at Ecole Centrale de Lyon. The developed geometry provides a high efficiency and a wide operability range as discussed in [16]. It is constructed from layered carbon fibre composites, with a structural analysis presented in [17]. The fan stage is currently fabricated and will be experimentally investigated within the European CleanSky-2 project CATANA (Composite Aeroelastics and Aeroacoustics, geometry available upon request under catana.ec-lyon.fr) in 2022. The global objective of this project is to analyse and improve the understanding of highly-coupled fluid-structure instabilities and to provide an open benchmark dataset for aeroelastic and aeroacoustic research.

In [16] and [17] time-averaged or time-linearized numerical methods were employed to assess performance and aeroelastic stability. In the current study, more advanced, time-accurate full annulus simulations have been used with the objective to capture the evolution of rotating-stall, small-scale aerodynamic disturbances and possible interaction mechanisms.

A detailed numerical investigation of the flow field at design speed and at aeroelastically more relevant part-speed condition has been carried out and is presented in this paper. Simulations show that under certain conditions three-dimensional vortical disturbances evolve, developing at the casing tip of the leading edge and convecting around the circumference, which are known as a potential source of NSV [14]. Based on these observations, a simple intentional aerodynamic mistuning geometry was introduced by varying the leading-edge sweep in an alternating assembly pattern, that can be easily realized in experiments and is expected to influence the onset of NSV. This type of mistuning will affect both the aerodynamic field near the casing, the propagation of disturbances and the structural eigenfrequencies.

A discussion is presented in this paper, including:

- a numerical study of aerodynamic performance in single- or dual-passage RANS simulations, with and without alternating sweep
- an analysis of the steady impact of an alternating sweep pattern on the flow structure in the fan
- the transition of RANS-simulations into full-annulus simulations with identical boundary conditions, with and without alternating sweep
- an analysis of the onset of aerodynamic instability at design- and part-speed
- the phenomenological difference induced by an alternating-sweep pattern.

2 Numerical set-up

The design of the fan stage with 16 composite rotor blades (diameter 508mm, design speed 11000rpm) and 31 outlet guide vanes (OGV) was presented in [16]. The nominal tip clearance is around $1mm$ corresponding to 1.1% of chord to ensure that fan blades do not touch the casing during stall inception and surge experiments. The computational domain for full-annulus simulations, shown in Fig. 1, considers the fan including a spherical inlet, intake, and a downstream annulus. As results show negligible influence of the far downstream located OGV, it is not modeled in the full annulus configuration. To facilitate numerical convergence at highly throttled conditions, a choked nozzle with variable section is introduced far downstream, comparable to the setup presented in [1]. A structured mesh has been created

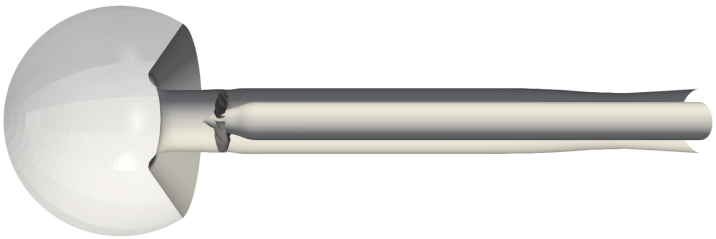

FIGURE 1. FULL-ANNULUS COMPUTATIONAL DOMAIN INCLUDING INLET, INTAKE, FAN AND CONVERGENT/DIVERGENT NOZZLE.

using AutoGrid5. Figure 2a shows the mesh of the spherical inlet, Fig. 2b presents a blade to blade view at the fan section and Fig. 2c shows a meridional view of the fan blade surface. The full-annulus domain is modeled with a total number of $53x10^6$ cells, with 133 layers in radial direction and 37 layers in the rotor tip gap, independent from the sweep-configuration. The wall resolution of this mesh is below $y^+ = 1$ for design conditions which corresponds to a mass flow rate of $\dot{m} = 36kg/s$ at design speed. In the downstream nozzle, a strong reduction of the axial discretization is applied to attenuate acoustic modes. The axial length of the last cell is $0.3m$ to provide a spatial filter for acoustic disturbances.

The flow solver is elsA, an unsteady Reynolds-Average Navier-Stokes solver developed by ONERA [18]. The Jameson scheme is used with second-order accuracy in space, as well as the $k-\omega$ Kok model to calculate turbulence. Unsteady simulations are time-accurate using a dual-time stepping scheme with 10 sub-iterations and 1920 physical time steps per revolution. This temporal discretization corresponds to 120 physical time steps per blade passing period and the highest frequency captured is $f = 960f_r$, equal to 60 times the fan blade passing frequency. As the inlet and the intake are defined in the stationary frame of reference compared to the fan domain which is described in the relative frame of reference, the interface between both domains is modeled with a sliding-mesh, instead of a mixing-plane in steady calculations. Steady-single and dual-passage results were used to initialized unsteady simulations. For steady and unsteady simulations, total pressure, total enthalpy and flow angles are specified at the intake. Static-pressure condition is applied at the exit, downstream of the choked nozzle, maintaining supersonic outlet flow in all simulations. Full-annulus calculations are distributed over 192 processors and performed for at least full 80 fan rotations to reach a periodic convergence state at near stall conditions.

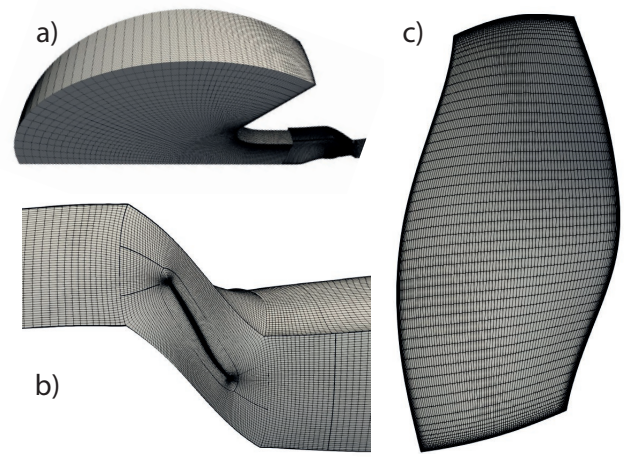

FIGURE 2. DETAILED VISUALIZATION OF STRUCTURED MESH FOR (a) INTAKE, (b) BLADE TO BLADE SECTION AND (c) FAN BLADE SURFACE.

3 Intentional aerodynamic mistuning

A previous study [15] based on reduced order model analysis shows that intentional mistuning is effective to suppress convective non-synchronous vibration, either by varying blade eigenfrequencies or by alternating the aerodynamic behaviour of individual blades. The relevant flow structures develop close to the casing, near the leading edge and propagate around the circumference due to high blockage in the passage. One obvious and simple possibility to introduce mistuning based on a fixed blade geometry is to alter the blade leading edge close to the tip, in a form that can be retrofitted to existing blades. Even though this type of geometry variation is known to be applied by different manufacturers, detailed studies are lacking in literature. In the presented study, an alternate pattern is applied by varying the sweep of the leading edge of every second blade. In [15] it is demonstrated, that the aerodynamic influence is mostly independent from the mistuning pattern, merely, structural mistuning is highly efficient in an alternating pattern for low mistuning amplitudes (1% frequency alternation). As stationary dual-passage RANS simulations are possible for this pattern, it was selected for the presented study.

Fig. 3 presents the baseline (BLADE-A) and the modified tip sections (BLADE-B) near the leading edge of the rotor blade. The leading edge shape is constant for both geometries, merely swept back by approximately 10% of chord with respect to the original blade. The modification starts around 85% of channel height ($85\%H$), smoothly evolving towards the tip.

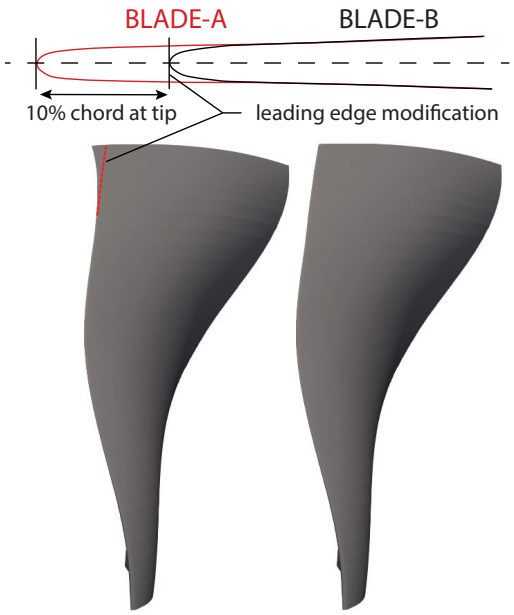

FIGURE 3. SCHEMATIC OF AERODYNAMIC MISTUNING, BLADE-A REPRESENTING BASELINE GEOMETRY, BLADE-B MODIFIED BLADE, ALTERNATE SWEEP PATTERN ASSEMBLED FROM 8 BLADES OF EACH GEOMETRY

4 Steady results

Fan performance map

Fig. 4 presents the fan-only total pressure ratio and isentropic efficiency at two rotation speeds (80% and 100% of the design speed) derived from single-passage steady simulations. A study including the OGV has shown negligible influence on both total pressure ratio and isentropic efficiency and is omitted in the figure.

The fan characteristic with the mistuned Alternate Sweep pattern is presented for design speed, depicted as red square symbols. Average performance from converged unsteady full-annulus simulations for the baseline and the mistuned configuration is depicted as hollow symbols.

The baseline characteristics present a general trend which is representative of UHBR Fans described in literature [1, 19–21]. At design speed, the fan operates at an isentropic efficiency above 90% in a wide range between 30.1 kg/s and 39.1 kg/s, with peak-efficiency exceeding 95%.

Five operating conditions will be discussed in this paper: OP-A, OP-B and OP-C at design speed and OP-D/OP-E at part-speed. OP-A corresponds to the design point with a massflow rate of $\dot{m} = 36$ kg/s and shows equivalent total pressure ratio and isentropic efficiency for steady and unsteady simulations. At OP-B strong unsteady aerodynamic disturbances are observed when switching to full-annulus URANS simulations as will be discussed. When the nozzle is slightly throttled (0.5% section change), a significant drop in total pressure ratio is observed towards OP-C in RANS, also visible in the isentropic efficiency. At part-speed, unsteady aerodynamic phenomena were also observed at OP-D and OP-E, but without the prominent performance drop as observed at OP-B.

As shown in Fig. 4, the introduction of an alternate pattern in the rotor geometry impacts steady performance of the fan at design speed. For the alternate sweep configuration, the drop in pressure ratio tends to increase with the reduction of the massflow rate. The alternating pattern causes a reduction of isentropic efficiency from 92.6% to 91.3% at OP-B. For high massflow rates, total pressure ratio and isentropic efficiency is degraded less through presence of alternating sweep (from 95.9% to 95.6% at OP-A).

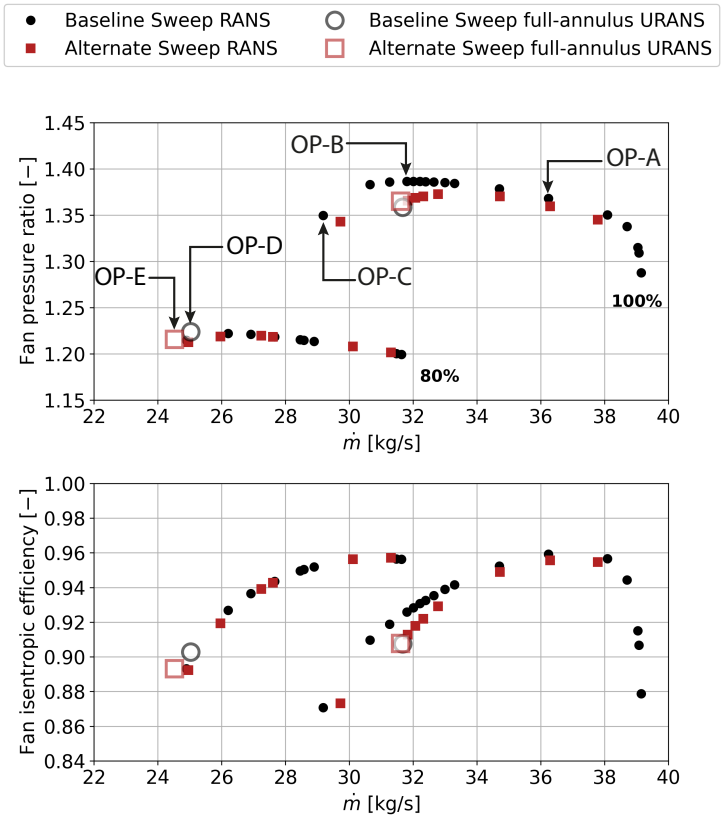

FIGURE 4. MASS-AVERAGED FAN CHARACTERISTICS AT 80% AND 100% OF THE DESIGN SPEED FROM STEADY AND UNSTEADY SIMULATIONS: TOTAL PRESSURE RATIO AND ISENTROPIC EFFICIENCY.

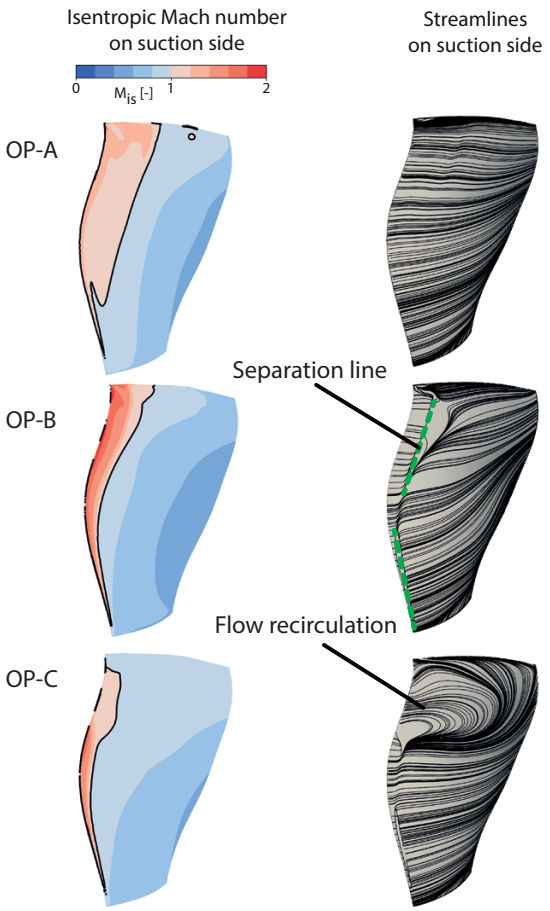

FIGURE 5. FLOW STRUCTURES AT DIFFERENT OPERATING POINTS AT DESIGN SPEED: OP-A, OP-B AND OP-C. ISENTROPIC MACH NUMBER DISTRIBUTION ON THE SUCTION SIDE WITH A BLACK ISOCONTOUR AT $M_{is} = 1$, STREAMLINES ON THE SUCTION SIDE

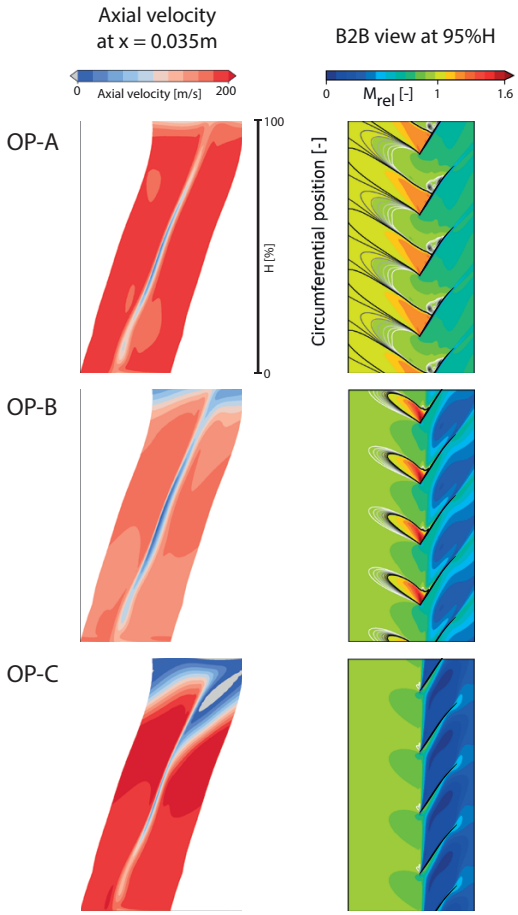

FIGURE 6. FLOW STRUCTURES AT DIFFERENT OPERATING POINTS AT DESIGN SPEED: OP-A, OP-B AND OP-C. AXIAL VELOCITY AT $x = 0.035m$ AND CONTOUR AT 95%H OF RELATIVE MACH NUMBER WITH GREY ISOCONTOURS AT LOW SUPERSONIC SPEED (1.0 TO 1.1) TO EMPHASIZE SHOCK STRUCTURE.

Steady flow structure at design speed From OP-A to OP-C, flow structures are presented in Fig. 5 by plotting the isentropic Mach number on the suction side and streamlines on the suction side. A shock structure is observed on the suction side at each operating point. At OP-B, the intensity of the shock strongly increases compared to OP-A. For OP-A and OP-B, the shock extends from midspan towards the blade tip. Regarding streamlines on the suction side, the flow is homogeneous at OP-A with traces of radial migration starting at the hub aligning with the trailing edge.

The visualization of axial velocity in Fig. 6 close to the trailing edge of the fan shows a thin boundary layer at the casing and a clearly defined wake induced by the rotor blade. The blade to blade view does not indicate a blockage zone in the blade passage at 95%H.

At OP-B, radial migration is stronger and a separation line (green dotted line) is observed near the leading edge between 40%H and 90%H. Downstream of the fan, the wake and the boundary layer at the casing are growing thicker with reduction of massflow. A wide blockage zone near the tip region is identified in the blade-to-blade view with a relative Mach number below 0.2. The shock topology at OP-C is different, its radial extent and intensity is reduced. A strong decrease of the fan pressure ratio is observed for this operating condition (see Fig. 4). The streamlines show a steady recirculation zone, with local backflow in the upper part of the channel. The radial migration at lower channel heights is less intense at this operating point. Visualization of the axial velocity field downstream of the rotor reveals a zone of negative velocity close to the casing.

The blockage in the tip region strongly increases with the reduction of the massflow rate and no shock structure is observed in the blade-to-blade view at 95%H . These results are

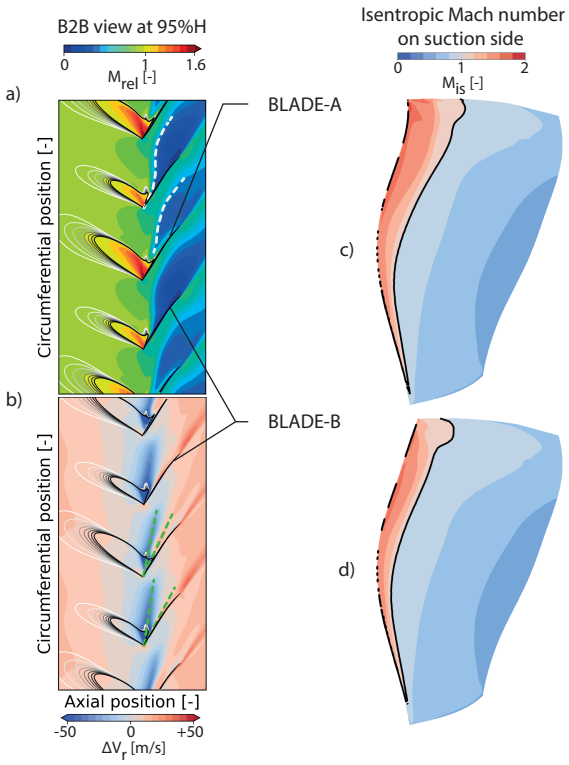

FIGURE 7. FLOW STRUCTURES AT OP-B FOR THE ALTERNATE SWEEP CONFIGURATION. CONTOURS AT 95%H OF RELATIVE MACH NUMBER (a), RADIAL VELOCITY (b) WITH GREY ISOCONTOURS AT LOW SUPERSONIC SPEED TO EMPHASIZE SHOCK STRUCTURE (a, b), AND ISENTROPIC MACH NUMBER DISTRIBUTION ON THE SUCTION SIDE (c, d) WITH A BLACK CONTOUR AT $M_{is} = 1$.

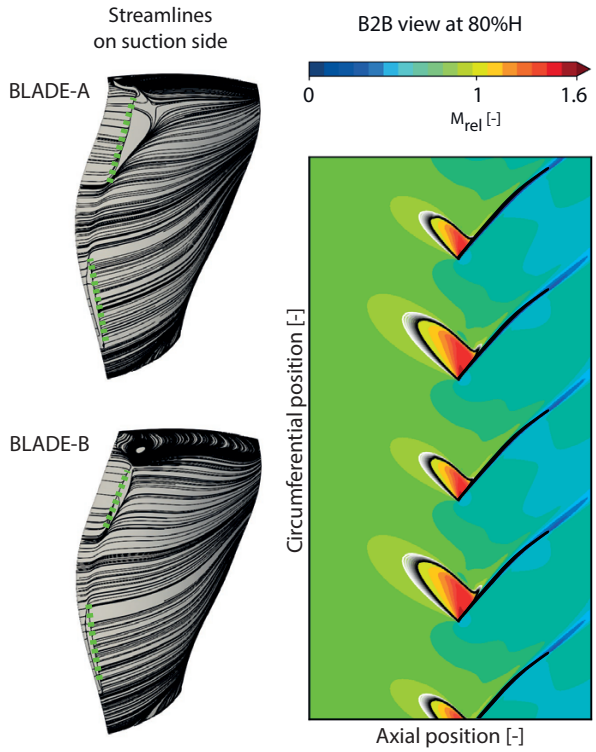

FIGURE 8. STREAMLINES ON THE SUCTION SIDE AT OP-B FOR THE MISTUNED CONFIGURATION AND CONTOUR OF RELATIVE MACH NUMBER AT 80%H WITH GREY ISOCONTOURS AT LOW SUPERSONIC SPEED TO EMPHASIZE SHOCK STRUCTURE.

presented for completeness, but obviously, a flow structure as simulated for OP-C will not be stable in experiments, and hence RANS simulations are not suitable for these conditions. Experiments and simulations presented in [1] for a comparable setup indicated significant differences for highly throttled conditions (OP-C). Close to peak pressure condition (comparable to OP-B) RANS and URANS simulations have proven accurate. Hence, the following analysis will concentrate on OP-B.

At OP-B, the RANS results are presented in Fig. 7 for the alternating sweep pattern, derived using dual-passage simulations with the same inlet and outlet conditions as for the tuned case. At this condition, the fan total pressure ratio and isentropic efficiency are slightly degraded compared to the tuned configuration (pressure ratio 1.39 vs 1.37, efficiency 93% vs 91%, comp. fig. 4)

Steady flow structures at OP-B for the mistuned configuration are presented in Fig. 7 by plotting the blade-to-blade view at 95%H contoured by the relative Mach number (a) and the radial velocity (b). The grey isocontours at low supersonic speed (Mach 1.0 to 1.1) reveal a comparable shock position on the suction side near the leading edge as observed in the tuned configuration but a strong blade-to-blade asymmetry of the shock topology. Blade-B shows a more concentrated supersonic expansion zone and particularly a larger blockage zone in the subsequent passage, as indicated by white dashed lines. The isentropic Mach number distribution on the suction side for both geometries (c, d) indicates that Blade-A has the same homogeneous Mach-number distribution as in the tuned baseline case, whereas Blade-B produces a significant dent in the shock close to the casing (black line), which can be attributed to interaction with tip-leakage flow. Influence of tip-leakage flow is visualized by the plot of radial velocity at 95%H in (b), superimposed by relative Mach-number contours to emphasize the shock. The reduced forward sweep of Blade-B causes the tip-leakage flow to be more inclined in circumferential direction, leading to a more pronounced zone of negative radial velocity upstream of the blockage zone.

These observations are coherent with previous studies [22, 23]. The introduction of a backward sweep in the tip blade geometry tends to increase losses and to produce increased blockage. Streamlines presented in Fig. 8 of BLADE-A resemble the tuned configuration shown in Fig. 5 with a strong radial mi-

gration from the hub towards the trailing edge. A flow separation line is inclined towards the shock, which is very different to Blade-B, showing a more concentrated separation around 80%H. The difference of flow structure is visualized in the blade-to-blade view in Fig. 8 at 80%H, contoured by the relative Mach number. Here, the blockage zone due to tip-leakage is not visible compared to Fig. 7 but the variation of shock intensity and extension of the supersonic zone is equally pronounced. This point is important, as the variation of leading edge geometry does not extend to this channel height, emphasizing the strong influence of the tip-leakage flow.

Radial profiles at design speed The fan pressure ratio and the total temperature rise downstream of the rotor blade are plotted against the channel height in Fig. 9 from OP-A to OP-C. At OP-A, the total pressure ratio is uniformly distributed over the channel height with a reduction towards the hub, which is typical for low speed fans with low hub-to-tip ratio. Throttled towards OP-B, the pressure ratio profiles increase above 50%H, hub-flow remains unaffected. A dent appears at 95%H due to the tip leakage flow (comp Fig. 5). At OP-C the increased tip-blockage causes a severe drop of pressure ratio above 60%H, with the hub still working at conditions comparable to OP-A. This change of operating condition concentrated to the high channel heights is equally pronounced in the work input, presented by the total temperature rise. Here it can be seen that OP-B and OP-C have the same maximum loading at the casing but only the work distribution between 60%H and 90%H shifts radially due to the changed tip-blockage situation.

To compare performance of the Alternate Sweep configuration, radial profiles are presented in Fig. 10 for OP-A and OP-B. No significant differences are observed at OP-A confirming that the total pressure ratio and the isentropic efficiency are marginally affected (see Fig 4). At OP-B, the fan pressure ratio is reduced above 40%H, showing an overall higher loading of the tuned configuration for the same throttle conditions, explaining the difference observed in Fig.4. Concluding, steady RANS simulations predict a severe total pressure ratio drop of the alternate pattern compared to the tuned case at loaded conditions, resulting from larger tip-blockage that affects the flow field down to 40%H of the channel height. A reduction of work near the casing is also induced by the tip-blockage. Design and peak-efficiency conditions are only slightly affected by the mistuning-pattern, with a loss of isentropic efficiency of 0.3%.

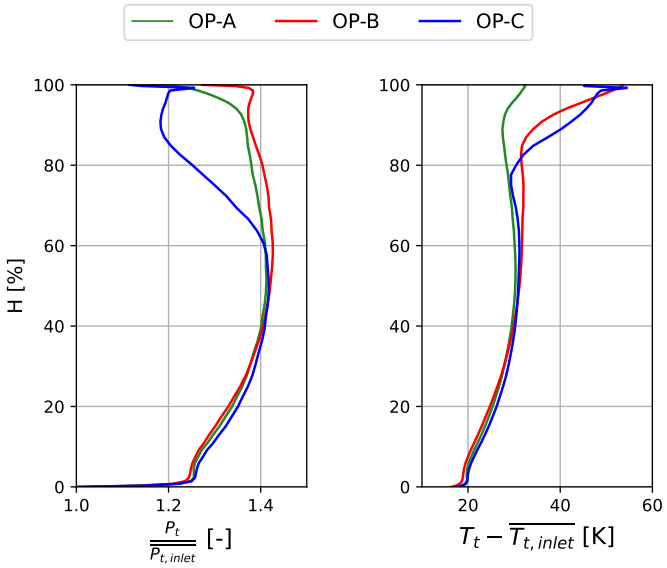

FIGURE 9. FAN TOTAL PRESSURE RATIO AND TOTAL TEMPERATURE RISE PROFILES AT $x = 0.05m$ DOWNSTREAM OF THE FAN FROM OP-A TO OP-C AT DESIGN SPEED.

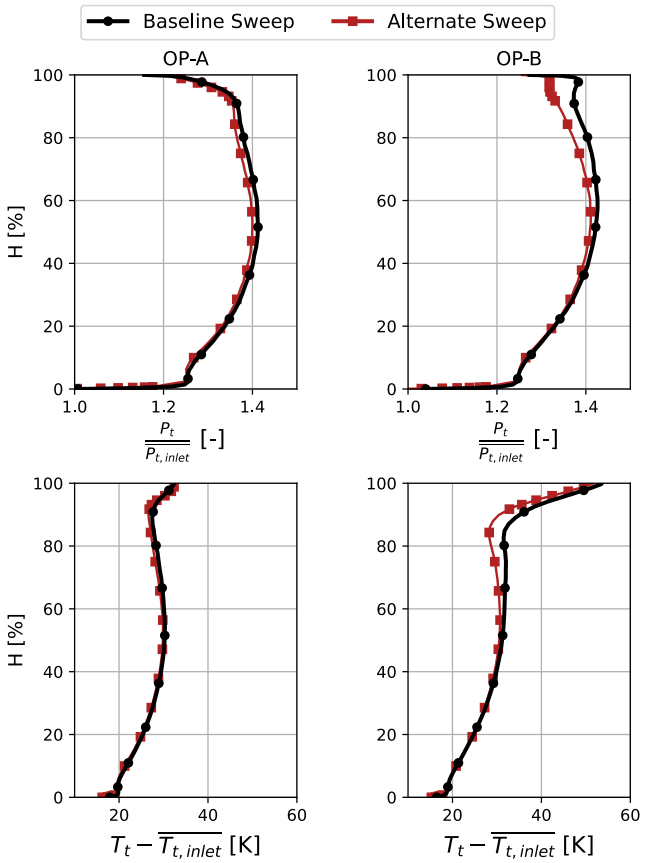

FIGURE 10. FAN TOTAL PRESSURE RATIO AND TOTAL TEMPERATURE RISE PROFILES AT $x = 0.05m$ DOWNSTREAM OF THE FAN FOR OP-A AND OP-B AT DESIGN SPEED FOR BASELINE AND ALTERNATE SWEEP RANS SIMULATIONS.

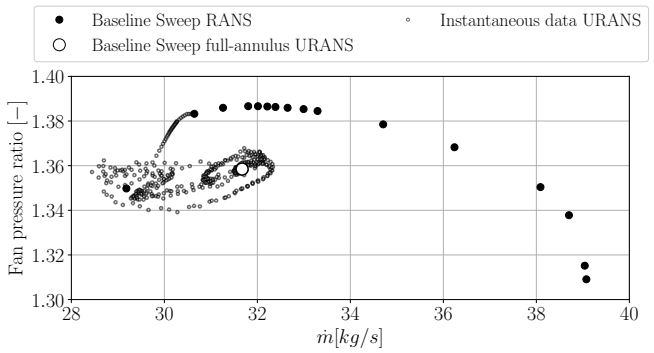

FIGURE 11. FAN PRESSURE RATIO AT DESIGN SPEED FROM STEADY AND UNSTEADY CALCULATIONS.

Aerodynamic stability analysis at design speed
Unsteady full-annulus simulations of the tuned configuration were started from converged RANS solutions. For all operating points near OP-B shown in the characteristic, the URANS simulation remains stable if the throttle condition remains constant. However, results presented by [1] for a low-speed fan have shown that significant differences of aerodynamic performance occurred between experiments and simulations as soon as the maximum pressure condition was surpassed. Hence, the stability of the aerodynamic solutions was investigated by transiently changing the throttle condition. The result of a simulation, where the throttle was slightly opened from a RANS point left of OP-B (throttle 67.5% of OGV outlet section) to the OP-B throttle conditions (68%) are presented in the following.

The transient fan pressure ratio during convergence is plotted in Fig. 11. A total of 80 rotations are calculated to ensure periodic convergence. A significant shift of operating conditions with a sharp drop of pressure ratio is observed until it converges towards the mass-flow of OP-B, but also with a significant loss in isentropic efficiency as observed in Fig. 4. The transient characteristics show that the simulation initially falls toward OP-C conditions and then re-stabilizes at higher mass-flow. The fan pressure ratio of the unsteady full-annulus simulation in Fig. 4 is time averaged over the last 10 converged rotations. Similar observations were observed in numerical simulations for rotating stall in a transonic fan [24].

Analyzing the transient flow field during this manoeuvre, small disturbances appear in the tip region, coalescing into two unequally distributed part-span rotating-stall cells after 10 fan rotations. Then, one of the two cells decreases in intensity until only one periodically propagating stall cell remains in the simulation after 50 fan rotations. To visualize, Fig. 12 shows an axial cut at 25% of chord and a blade-to-blade view at 95%H over the entire circumference contoured by the axial velocity field after 20 and 60 fan rotations, representing a transient case with dual-cells and the periodically converged single part-span stall cell, both

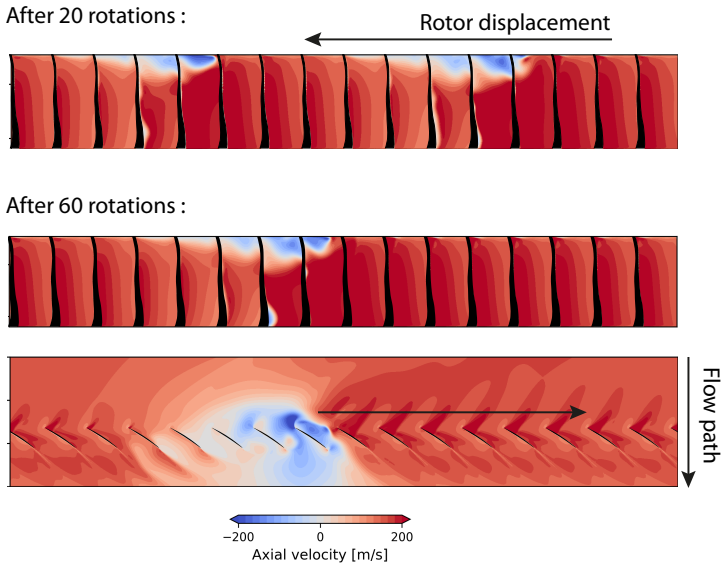

FIGURE 12. AXIAL CUT AT 25% OF CHORD, AFTER 20 AND 60 ROTATIONS, AND CONTOUR OF AXIAL VELOCITY AT 95%H at $t = 60$ ROTATIONS AT OP-B FROM URANS SIMULATION.

with a large zone of negative axial velocity close to the casing. In addition, a flow separation near the hub is also visible in the simulation, which is travelling with the same speed and in the same direction as the casing cell. These results are of particular interest, as the operating point from which the simulation was started is well within the operating range predicted by RANS simulations and the throttle was even opened from this condition. The simulation can recover mass-flow towards OP-B condition and does never enter full-span stall, but the remaining stall cell persists after longer convergence at constant amplitude. Hence we conclude, that condition OP-B and lower mass-flows in RANS is a particularly unstable configuration, that - if disturbed - can stabilize onto a lower pressure ratio condition at equal mass-flow but with a pronounced part-span rotating stall cell. Similar results have been obtained for different throttling procedures and the converged state is independent from the initial condition.

Fig. 13 presents the time averaged radial profiles of the converged solution at OP-B compared to the RANS simulation. It can be seen, that the total pressure level is affected from 40%H to the casing. Close to the casing the average work input is significantly reduced. This operating condition is very critical for experimental investigations. Both curves are only slightly affected (in contrast to typical full-span rotating stall), but the propagating cell will lead to significant aeroelastic forcing.

To quantify the strength of the stall-cells, the non-synchronous signals of two numerical probes located in the same passage near the leading edge are plotted during the last 10 converged rotations in Fig. 14. The presented signals show static pressure amplitudes of 20 kPa, representing approximately 1.5

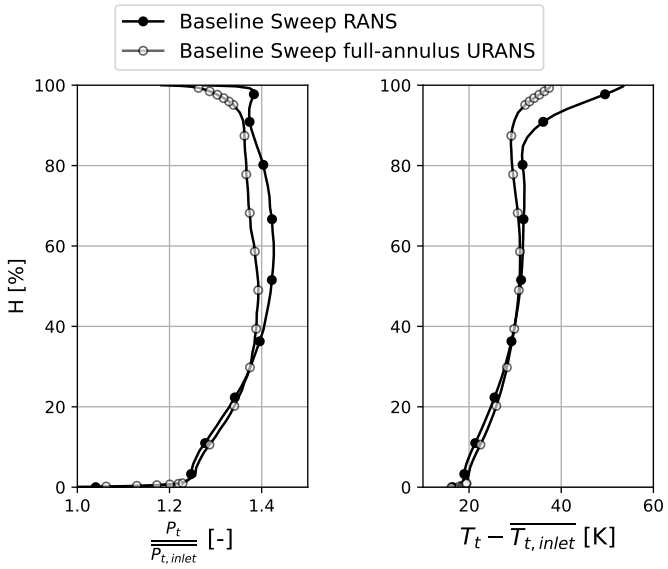

FIGURE 13. FAN TOTAL PRESSURE RATIO AND TOTAL TEMPERATURE RISE PROFILES AT $x = 0.05m$ DOWNSTREAM OF THE FAN FOR OP-B AT DESIGN SPEED FROM RANS AND TIME AVERAGED URANS SIMULATIONS.

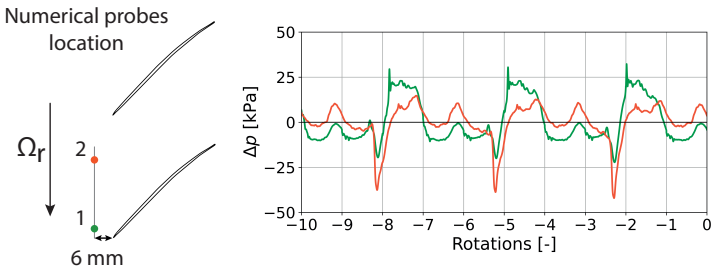

FIGURE 14. NUMERICAL PROBES LOCATION NEAR THE LEADING EDGE AT 80%H AND NON-SYNCHRONOUS STATIC PRESSURE SIGNALS IN THE ROTATING FRAME OF REFERENCE AT PERIODICALLY CONVERGED CONDITION AT OP-B.

times the dynamic head at stage inlet (13 kPa at OP-B).

The propagation speed of the cells is determined as 31% of the rotor speed in the rotating frame of reference, independent from a dual or single cell configuration. Hence, blade excitation will occur at multiples of 0.31EO. At design speed, the FEM-predicted frequencies of the first three eigenmodes are 1.42EO, 3.64EO and 4.87EO respectively, hence only the fourth and higher harmonics of the stall cell could lead to resonance with the first flap mode. However, if a multi-cell configuration establishes in experiments, this phenomenon can become critical and must be under close surveillance.

To conclude on these simulations, a very critical phenomenon has been observed: RANS simulations as well as URANS with untriggered instability sources predict a significantly higher performance for this type of perfectly symmetric and tuned low-speed fans at throttled conditions. From an aerodynamic point of view, a secondary, periodically stable condition is determined but involving propagating part-span cells of significant amplitude, whose actual cell number can be decisive for resonant blade vibration. To produce this result, artificial triggers are necessary in the simulation, either by transient throttling or for example through mis-staggered blades [13].

Introduction of aerodynamic mistuning at Design speed In the same way as for the tuned fan, full-annulus unsteady simulations of the alternatingly mistuned configuration were performed at the OP-B conditions. Here, the transient simulation directly leads to the establishment of part-span stall without the necessity of a throttle-trigger as for the tuned case. After reaching periodic convergence, the rotating stall characteristics are comparable to those observed in the tuned configuration for the same operating conditions, as shown in Fig. 4. For the same massflow rate corresponding to OP-B, the mistuned configuration has the same performance as the tuned case. This is of relevance, as compared to the steady RANS characteristic of the dual-passage model the drop of pressure ratio and efficiency is negligible. In contrast to the tuned case, the periodic state presents an inhomogeneous dual-cell configuration, as can be seen in Fig. 15. The temporal evolution of a blade-to-blade view at 95%H contoured by the axial velocity during one rotation in the rotating frame of reference is plotted for both configurations.

Fig. 16 presents the time averaged amplitude over the last 10 converged rotations of the circumferential decomposition of the axial velocity near the leading edge at 95%H for the baseline and the alternate sweep configuration. For both configurations the blade count $N_a = 16$ and its 2^{nd} harmonic are observed in the decomposition. For the baseline sweep configuration, a broadband activity at low circumferential wave numbers with a dominant wave number at $N_a = 2$ is identified. This activity is induced by the establishment of contra-rotating part-span stall cells, as discussed before. Regarding the mistuned configuration, the amplitude of this disturbance is strongly reduced. Thus, the cell intensity is reduced through the alternating pattern, but propagation speed is similar.

Hence, against intuition, the mistuned case presents a more predictable case for throttled conditions. Steady RANS simulations directly evolve aerodynamic instabilities without artificial triggers when switched to URANS and the associated performance drop is less severe than for the tuned case.

This implies that all simulations based on converged steady RANS solutions, such as time-linearized stability investigations, must be analysed with caution. Also, design optimization of respective geometries can be misleading when based solely on RANS-approaches.

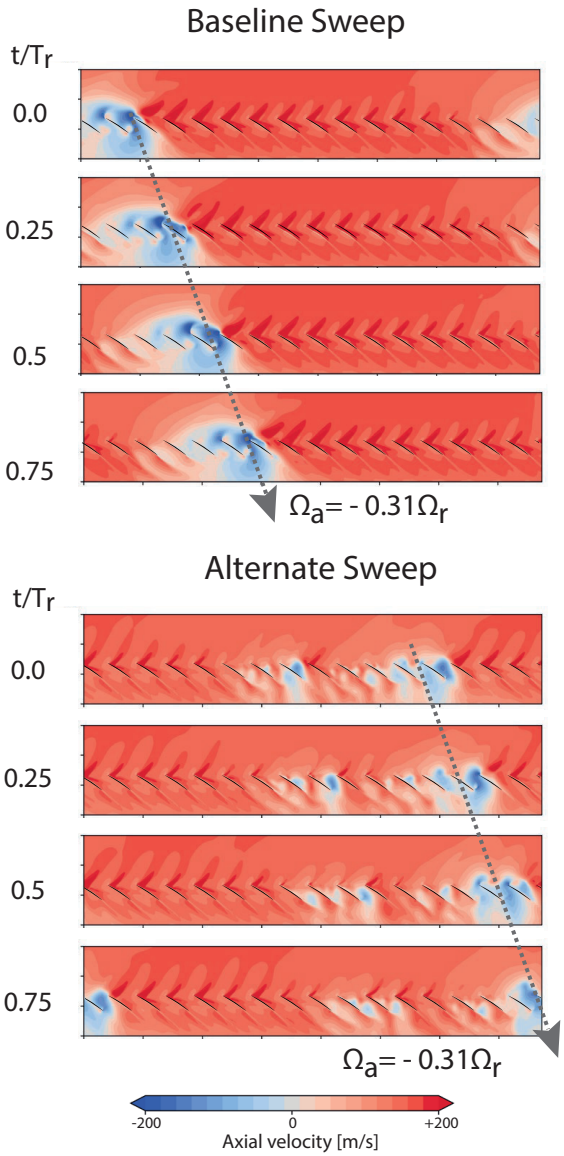

FIGURE 15. TEMPORAL EVOLUTION OF BLADE-TO-BLADE VIEW AT 95% OF CHANNEL HEIGHT CONTOURED BY AXIAL VELOCITY AT OP-B AT 100% OF DESIGN SPEED FOR BASELINE AND ALTERNATE SWEEP CONFIGURATION FROM URANS SIMULATIONS: A PART-SPAN ROTATING STALL CELL PROPAGATES IN THE OPPOSITE DIRECTION OF THE ROTOR.

5 Part-Speed Analysis

In [17], a time-linearized study of aeroelastic stability has shown a critical condition near OP-D at 80% part-speed conditions, related to a convective phenomenon in the leading edge tip region. To examine the nature of the instability described in [17], time-accurate URANS, full annulus simulations have been conducted.

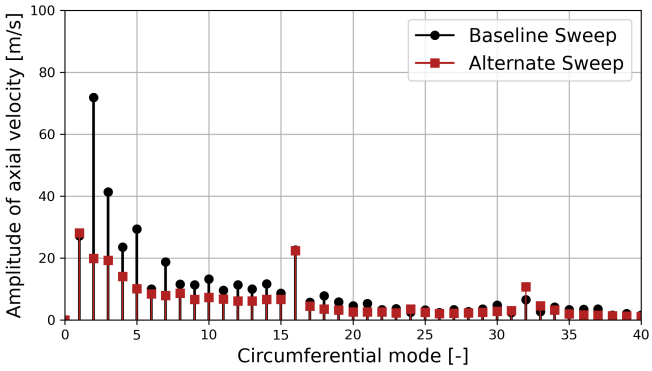

FIGURE 16. CIRCUMFERENTIAL DECOMPOSITION OF THE AXIAL VELOCITY NEAR THE LEADING EDGE AT 95%H FOR BASELINE AND ALTERNATE SWEEP CONFIGURATION FROM URANS SIMULATIONS (TIME AVERAGE OVER 10 CONVERGED ROTATIONS).

As seen in the fan characteristics (Fig. 4) the unsteady simulations, started from equal mass-flow for each configuration converge to slightly different operating conditions. The baseline case increases mass-flow, pressure-ratio and efficiency compared to the RANS-solution. The alternate sweep configuration, which has almost identical total pressure ratio (and isentropic efficiency) in RANS, converges towards OP-E at lower mass-flow, but marginally increased pressure ratio and efficiency. Analysis of the radial profiles in Fig.17 confirms that the unsteady, converged solutions are equal to the Baseline Sweep RANS configuration up to 60%H. Close to the casing, both configurations produce higher total pressure ratio compared to RANS with advantages for the baseline configuration.

Flow-field analysis of the baseline configuration at OP-D reveals the establishment of small-scale disturbances. Fig. 18 presents the temporal evolution of the axial velocity on a blade-to-blade view at 95%H in the rotating frame of reference during one period of the aerodynamic disturbance. A small-scale perturbation arises on the suction side and propagates toward the pressure side of the adjacent blade in the circumferential direction at a speed of $-0.37\Omega_r$. Since all blades are identical, the onset of disturbances is synchronized around the circumference with a wave-number equal to the number of blades $N_a = N_b = 16$.

To analyze the 3-dimensional structure of the disturbances, Fig. 19 illustrates isocontours of the Q-criterion during one blade passing period of the disturbances. The Q-criterion is considered to emphasize the vortex structures observed in the inter-blade passage. At instant $t = 0.0T_{fan}$, a small vortical structure is observed near the leading edge close to the casing. In the following snapshots, the structure (circled in red) grows and extends further towards the trailing blade. Eventually the blade bound leg detaches from the blade and the vortex is convected upstream of

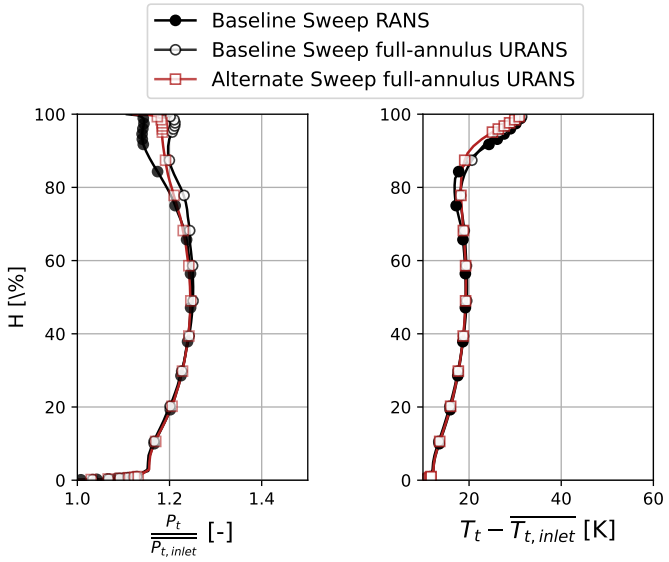

FIGURE 17. RADIAL PROFILES AT 80% PART SPEED, STEADY RANS FOR BASELINE CONFIGURATION, TIME AVERAGE URANS FOR BASELINE AND ALTERNATE SWEEP CONFIGURATION.

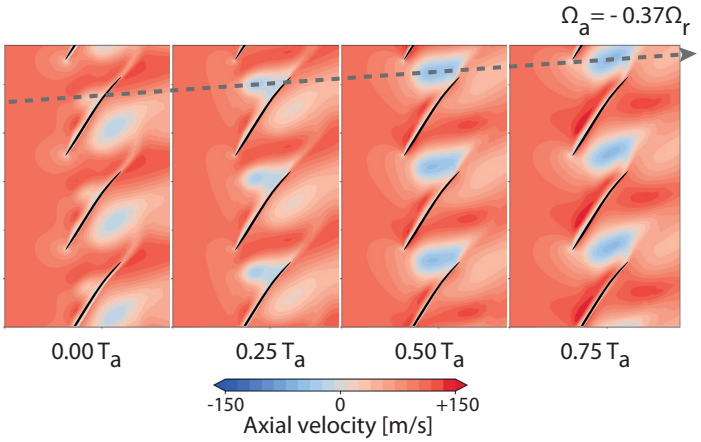

FIGURE 18. TEMPORAL EVOLUTION OF A BLADE-TO-BLADE VIEW AT 95% OF CHANNEL HEIGHT CONTOURED BY AXIAL VELOCITY AT OP-D AT 80% OF DESIGN SPEED: SMALL DISTURBANCES PROPAGATE IN THE CIRCUMFERENTIAL DIRECTION.

the blockage zone around the circumference. To visualize the periodically stable convection of the disturbances, Fig. 20 shows how the local entropy signal at 25% of the chord at 95%H of channel height develops during the unsteady simulation, starting from steady RANS condition at Rotation 0. After approximately three rotor revolutions an homogeneous and periodic pattern evolves, propagating at -37% of rotor speed against rotation with a constant wave number of $N_a = N_b = 16$.

This form of small-scale disturbances, convecting at constant speed is known to lead to convective NSV phenomenon if they adapt their phase to structural blade oscillation [14]. Numerous convective NSV cases have been reported these past decades in high-speed compressors [6,8] and low-speed fans [1], in which similar convected flow structures established at highly-loaded operating conditions as those observed at OP-D. Literature indicates that this form of disturbances is convected at constant speed without blade vibration. Onset of NSV leads to lock-in with a vibration pattern and a slight shift in propagation speed.

The alternate sweep configuration behaves different at this operating condition. Also starting from converged RANS at OP-D, an initially transient aerodynamic disturbance with a high wave number evolves and propagates around the circumference. Between 2 and 6 revolutions, the pattern resembles the tuned case, but after approximately 8 revolutions, individual cells form, developing a periodically converged dual-cell part span-stall pattern, which only marginally penalizes fan performance, as discussed before.

This result at part speed is of even greater importance than the effect of alternate sweep at design speed. The experiments reported by [1] have shown that for a comparable low-speed fan, NSV can be the limiting factor for the operating range at part speed conditions, triggered by convected disturbances upstream of the blockage zone. The results of [17] on the fan used for the present study, based on time-linearized simulations at part speed have shown that instability of the second Eigenmode in Nodal Diameter $N_v = 5$ is predicted near OP-D, at a structural eigenfrequency $\omega_v/\Omega_r = 4.32EO$. These simulations assume a fixed eigenfrequency, and Nodal Diameter 5 can be coherent with an aerodynamic wave number of 11, aliased on a 16 bladed rotor [14]. In this case, the aerodynamic disturbance would propagate at a speed of $\Omega_a/\Omega_r = \omega_v/(\Omega_r N_a) = 4.32EO/11 = 0.39$.

The results presented here show that small-scale convected disturbances propagate continuously with a free convection speed of $\Omega_a/\Omega_r = 0.37$ without forced blade vibration, hence proving that convective NSV is the cause for the instability observed in [17], and particularly, that disturbance characteristics and propagation are independent from blade vibration.

As can be seen in Fig. 20 b) for the aerodynamically mistuned case, the small scale disturbances disappear and evolve into low wave number part-span stall. This phenomenon is much less severe from an aeroelastic point of view as frequencies in the relative frame are lower, reducing the possibility for lock-in. As the fan can still operate at sufficient aerodynamic performance despite the part-span stall, this provides an efficient countermeasure against NSV. Additionally to this, the structural mistuning, which will be induced by the alternate sweep, will further reduce the sensitivity towards NSV as reported in [15]. Estimations based

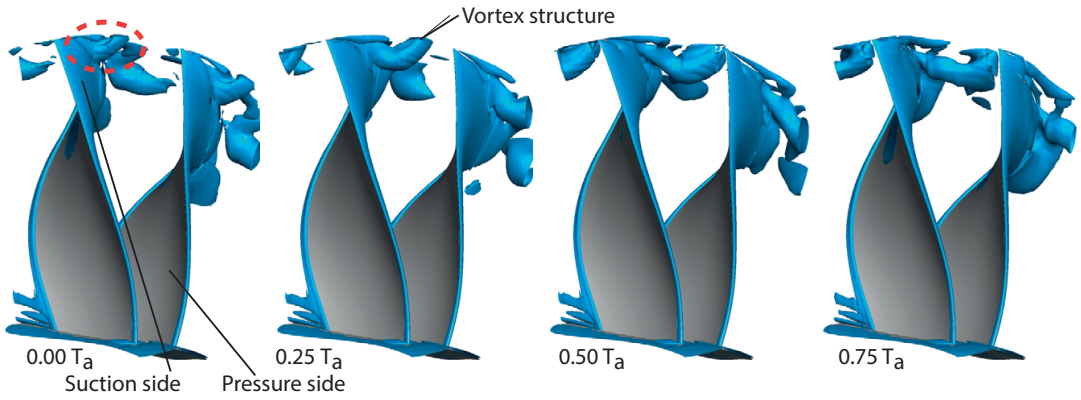

FIGURE 19. VISUALIZATION OF VORTEX STRUCTURES DURING ONE PERIOD OF AERODYNAMIC DISTURBANCES, ISO-CONTOUR AT Q-CRITERION $= 2 \cdot 10^7$, VALUES BLANKED ABOVE 99%H, URANS SIMULATION AT OP-D.

on FEM-simulations indicate a frequency shift of approximately 5% for the torsional mode between Blade-A and B. Hence, combined optimizations considering both aerodynamic and structural mistuning are possible to improve aeromechanical stability and maintaining aerodynamic performance.

6 Conclusions

Unsteady aerodynamic phenomena have been numerically observed in the open-test-case fan ECL5 which is representative of a near-future UHBR fan concepts with carbon-fibre composite blades. Two relevant speedlines have been investigated in this paper with steady and unsteady full-annulus simulations, including an intentional aerodynamic mistuning pattern.

At design speed, numerical simulations show discrepancies between steady and unsteady RANS for throttled conditions. The tuned configuration shows high fan pressure ratio and isentropic efficiency that remains stable in transient simulations as long as no disturbance is applied. Transient un-throttling triggers the onset of an initially symmetric blade stall that evolves rapidly into single-cell part-span stall with stable but reduced aerodynamic performance. Aeroelastic resonance is not indicated for the simulated results, but the possibility for stall-driven vibration involving a multi-cell configuration must be under surveillance in experiments. Applying an alternating forward sweep pattern leads to a slightly reduced fan performance with efficiency penalties at design point of approximately 0.3%. This result was expected as the geometry was intentionally altered towards a backward swept tip which is known to be detrimental for the development of tip-blockage. At throttled conditions the setup equally develops part-span stall but with higher pressure ratio and isentropic efficiency compared to the tuned case. In contrast to the tuned case, this does not require an artificial trigger. Hence, the mistuned configuration is more predictable at this condition.

At part-speed condition (80%), the tuned case develops small-scale aerodynamic disturbances with a vortex structure that evolves between the blade suction side and the casing within the operating range predicted by RANS calculations. These vortices travel around the circumference at a speed of $-0.37\Omega_r$ in the rotating frame of reference. This type of disturbance is known to be relevant for the occurrence of non-synchronous vibrations due to lock-in with a structural eigenmode. Throttling to higher loaded conditions, unsteady simulations show the establishment of a single rotating-stall cell. Introduction of mistuning has negligible

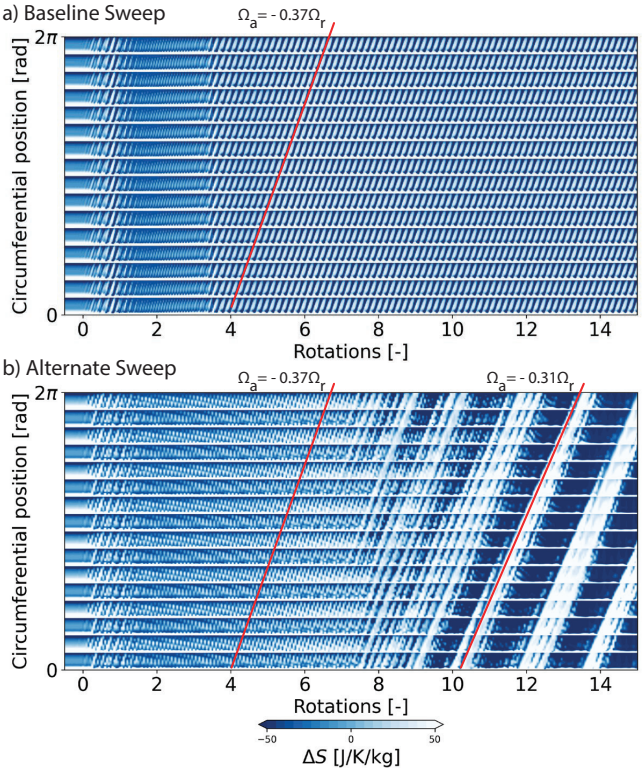

FIGURE 20. TRANSIENT SOLUTION OF THE AXIAL VELOCITY AT 0.75 OF CHORD AT 95%H IN THE ROTATING FRAME OF REFERENCE AT OP-D AND OP-E FROM URANS SIMULATIONS.

influence on fan pressure ratio and efficiency at part-speed conditions, but the traveling vortical disturbances evolve into low-amplitude part-span stall cells, which are known to be less critical for non-synchronous vibration. Hence, the presented mistuning configuration, which can be easily obtained by modifying existing blades presents a promising solution to suppress the tendency of the fan towards non-synchronous vibration at part-speed condition. Also, the setup is numerically more predictable, developing unsteady flow features without artificial triggers. However, aerodynamic performance penalties are observed. It is expected, that through intentional dual-blade design the efficiency decrease can be reduced, but maintaining aeroelastic benefits.

ACKNOWLEDGMENT

The authors are grateful for the technical advice and contributions of Stephane Aubert, Benoit Paoletti, Pascal Ferrand and Valdo Pages.

This project has received funding from the Clean Sky 2 Joint Undertaking (JU) under grant agreement N° 864719. The JU receives support from the European Union's Horizon 2020 research and innovation program and the Clean Sky 2 JU members other than the Union. This publication reflects only the author's view and the JU is not responsible for any use that may be made of the information it contains. The development of the Open Test Case rotor is supported by CIRT (Consortium Industrie-Recherche en Turbomachine). Numerical studies were supported by GENCI granting access to CINES through allocation DARI num. A0102A07410.

REFERENCES

[1] Rodrigues, M., Soulat, L., Paoletti, B., Ottavy, X., and Brandstetter, C., 2021. "Aerodynamic investigation of a composite low-speed fan for uhbr application". *J. Turbomach.,* ***143***(10), p. 101004.

[2] Emmons, H., 1955. "Compressor surge and stall propagation". *Trans. of the ASME,* ***77***(4), pp. 455–467.

[3] Baumgartner, M., Kameier, F., and Hourmouziadis, J., 1995. "Non-engine order blade vibration in a high pressure compressor". In Proc. 12th ISABE (International Society for Air Breating Engines).

[4] Kameier, F., and Neise, W., 1997. "Rotating blade flow instability as a source of noise in axial turbomachines". *J. Sound Vib.,* ***203***(5), pp. 833–853.

[5] Mailach, R., Lehmann, I., and Vogeler, K., 2001. "Rotating instabilities in an axial compressor originating from the fluctuating blade tip vortex". *J. Turbomach.,* ***123***(3), pp. 453–460.

[6] Kielb, R. E., Barter, J. W., Thomas, J. P., and Hall, K. C., 2003. "Blade excitation by aerodynamic instabilities: A compressor blade study". In Proc. ASME Turbo Expo 2003, pp. 399–406.

[7] Dodds, J., and Vahdati, M., 2015. "Rotating stall observations in a high speed compressor—part i: Experimental study,". *J. Turbomach.,* ***137***(5), pp. 51002–51010.

[8] Brandstetter, C., Juengst, M., and Schiffer, H.-P., 2018. "Measurements of radial vortices, spill forward, and vortex breakdown in a transonic compressor". *J. Turbomach.,* ***140***(6), p. 061004.

[9] Zhao, F., Dodds, J., and Vahdati, M., 2021. "Influence of blade vibration on part-span rotating stall". *International Journal of Gas Turbine, Propulsion and Power Systems,* ***12***(2), pp. 1–7.

[10] Inoue, M., Kuroumaru, M., Tanino, T., and Furukawa, M., 2000. "Propagation of multiple short-length-scale stall cells in an axial compressor rotor". *J. Turbomach.,* ***122***(1), pp. 45–54.

[11] Yamada, K., Kikuta, H., Iwakiri, K.-i., Furukawa, M., and Gunjishima, S., 2013. "An explanation for flow features of spike-type stall inception in an axial compressor rotor". *J. Turbomach.,* ***135***(2), p. 21023.

[12] Young, A., Day, I., and Pullan, G., 2013. "Stall warning by blade pressure signature analysis". *J. Turbomach.,* ***135***(1), p. 11033.

[13] Pullan, G., Young, A. M., Day, I. J., Greitzer, E. M., and Spakovszky, Z. S., 2015. "Origins and structure of spike-type rotating stall". *J. Turbomach.,* ***137***(5), pp. 51007–51011.

[14] Stapelfeldt, S., and Brandstetter, C., 2020. "Non-synchronous vibration in axial compressors: Lock-in mechanism and semi-analytical model". *J. Sound and Vibration,* ***488***, p. 115649.

[15] Stapelfeldt, S., and Brandstetter, C., 2021. "Suppression of non-synchronous-vibration through intentional aerodynamic and structural mistuning". *J. Turbomach.*

[16] Brandstetter, C., Pages, V., Duquesne, P., Ottavy, X., Ferrand, P., Aubert, S., and L., B., 2021. "Uhbr open-test-case fan ecl5/catana, part 1 : Geometry and aerodynamic performance". In Proc. 14th European Conference on Turbomachinery Fluid dynamics and Thermodynamics, ETC2021-626.

[17] Pages, V., Duquesne, P., Ottavy, X., Ferrand, P., Aubert, S., Blanc, L., and Brandstetter, C., 2021. "Uhbr open-test-case fan ecl5/catana, part 2 : Mechanical and aeroelastic stability analysis". In Proc. 14th European Conference on Turbomachinery Fluid dynamics and Thermodynamics, ETC2021-625.

[18] Cambier, L., Heib, S., and Plot, S., 2013. "The onera elsa cfd software: input from research and feedback from industry". *Mechanics & Industry,* ***14***(3), pp. 159–174.

[19] Lee, K.-B., Wilson, M., and Vahdati, M., 2017. "Numerical study on aeroelastic instability for a low-speed fan". *J. Turbomach.,* ***139***(7).

[20] Kim, S., Pullan, G., Hall, C. A., Grewe, R. P., Wilson, M. J., and Gunn, E., 2019. "Stall inception in low-pressure ratio fans". *Journal of Turbomachinery,* ***141***(7), 02.

[21] Brandstetter, C., Paoletti, B., and Ottavy, X., 2019. "Compressible modal instability onset in an aerodynamically mistuned transonic fan". *J. Turbomach.,* ***141***(3), p. 031004.

[22] Sasaki, T., and Breugelmans, F., 1998. "Comparison of sweep and dihedral effects on compressor cascade performance". *Journal of Turbomachinery,* ***120***(3), pp. 454–463.

[23] Place, J. M. M., and Cumpsty, N. A., 1998. "Discussion: Comparison of sweep and dihedral effects on compressor cascade performance (sasaki, t., and breugelmans, f., 1998, journal of turbomachinery, 120, pp. 454-463)". *Journal of Turbomachinery,* ***120***(3), pp. 463–464.

[24] Choi, M., Smith, N. H. S., and Vahdati, M., 2012. "Validation of numerical simulation for rotating stall in a transonic fan". *Journal of Turbomachinery,* ***135***(2).

The presented research was supported through Clean Sky 2 Joint Undertaking (JU), project CATANA under grant agreement N◦864719. The JU receives support from the European Union's Horizon 2020 research and innovation programme and the Clean Sky 2 JU members other than the Union. This publication reflects only the author's view and the JU is not responsible for any use that may be made of the information it contains.

catana.ec-lyon.fr
Christoph.brandstetter@ec-lyon.fr